coatings

MDPI

Article

Biodegradable Mg/HA/TiO$_2$ Nanocomposites Coated with MgO and Si/MgO for Orthopedic Applications: A Study on the Corrosion, Surface Characterization, and Biocompatability

Shahrouz Zamani Khalajabadi [1,2,*], **Aminudin Bin Haji Abu** [1,*], **Norhayati Ahmad** [2], **Mohammed Rafiq Abdul Kadir** [3], **Ahmad Fauzi Ismail** [4], **Rozita Nasiri** [5], **Waseem Haider** [6] and **Norizah Bt Hj Redzuan** [2]

[1] Malaysia-Japan International Institute of Technology (MJIIT), Universiti Teknologi Malaysia (UTM), Kuala Lumpur 54100, Malaysia

[2] Department of Materials, Manufacturing and Industrial Engineering, Faculty of Mechanical Engineering, Universiti Teknologi Malaysia (UTM), Johor Bahru 81310, Malaysia; nhayatiahmad@utm.my (N.A.); norizah@utm.my (N.B.H.R.)

[3] Medical Devices and Technology Group (MEDITEG), Faculty of Biosciences and Medical Engineering, Universiti Teknologi Malaysia (UTM), Johor Bahru 81310, Malaysia; rafiqu@yahoo.com

[4] Advanced Membrane Technology Research Center (AMTEC), Universiti Teknologi Malaysia (UTM), Johor Bahru 81310, Malaysia; behroozzamani1324@yahoo.com

[5] Faculty of Chemical Engineering, Universiti Teknologi Malaysia (UTM), Johor Bahru 81310, Malaysia; rozfish4524@gmail.com

[6] School of Engineering and Technology, Central Michigan University, Mount Pleasant, MI 48859, USA; waseem@gmail.com

* Correspondence: zkshahrouz2@liveutm.onmicrosoft.com (S.Z.K.); aminudin.kl@utm.my (A.B.H.A.)

Abstract: In the field of orthopedics, magnesium (Mg) and magnesium-based composites as biodegradable materials have attracted fundamental research. However, the medical applications of magnesium implants have been restricted owing to their poor corrosion resistance, especially in the physiological environment. To improve the corrosion resistance of Mg/HA/TiO$_2$ nanocomposites, monolayer MgO and double-layer Si/MgO coatings were fabricated layer-by-layer on the surface of a nanocomposite using a powder metallurgy route. Then, coating thickness, surface morphology, and chemical composition were determined, and the corrosion behavior of the uncoated and coated samples was evaluated. Field-emission scanning electron microscopy (FE-SEM) micrographs show that an inner MgO layer with a porous microstructure and thickness of around 34 μm is generated on the Mg/HA/TiO$_2$ nanocomposite substrate, and that the outer Si layer thickness is obtained at around 23 μm for the double-layered coated sample. Electrochemical corrosion tests and immersion corrosion tests were carried out on the uncoated and coated samples and the Si/MgO-coated nanocomposite showed significantly improved corrosion resistance compared with uncoated Mg/HA/TiO$_2$ in simulated body fluid (SBF). Corrosion products comprising Mg(OH)$_2$, HA, Ca$_3$(PO$_4$)$_2$, and amorphous CaP components were precipitated on the immersed samples. Improved cytocompatibility was observed with coating as the cell viability ranged from 73% in uncoated to 88% for Si/MgO-coated Mg/HA/TiO$_2$ nanocomposite after nine days of incubation.

Keywords: Mg/HA/TiO$_2$ nanocomposite; biodegradation behavior; Si/MgO; corrosion products; cytocompatibility

1. Introduction

In recent years, following the biodegradability of magnesium (Mg) alloys in the physiological body environment, their excellent biocompatibility especially osteopromotion, as well as the similar mechanical properties to human bone has led to biodegradable magnesium alloys and magnesium-based composites being considered for use as orthopedic implant materials over other traditional metallic materials [1–8]. However, the main limitation is the initial fast degradation of Mg alloys in a biological environment which could not afford effective biomechanical support and match the bone reconstruction [9,10]. In addition to the high corrosion rate, the low bioactivity of magnesium implants such as the ability to form hydroxyapatite (HA) is another challenging problem, which needs to be resolved before utilization in clinical applications [11–14]. To overcome this drawback, several surface modification techniques, i.e. electrochemical deposition [15,16], polymer treatment [17,18], chemical deposition [19,20], and micro-arc oxidation (MAO) techniques [21–23], have been introduced to improve the degradation rate and bioactivity of magnesium and its alloys [9,24]. As is known, fabrication of magnesium-based composites with bio-ceramic additives [25], besides the surface modification of magnesium implants, and alloying magnesium with biocompatible metals [26,27] are the major techniques to protect the implant from fast corrosion and degradation in vivo. Moreover, bio-additives and suitable coatings can improve the hemocompatibility and bioactivity of implants in this field [11,14,28–31]. Gu et al. [32] reported that pure Mg as the matrix materials, and HA as the bio-ceramic additive, were selected to fabricate the Mg/HA biocomposite with different amounts of HA content using the powder metallurgy (PM) route. The cytotoxicity tests indicated that Mg/10HA extract showed no toxicity to L-929 cells.

In a recent study, the addition of HA and TiO_2 caused a significant improvement in corrosion resistance and ductility of magnesium-based nanocomposites for medical applications. According to the cell culture results, the Mg/HA/TiO_2 nanocomposite was biocompatible with osteoblasts [33]. As was reported by Li et al. [34], the silicon coating was deposited on the surface of WE43 Mg alloy using Plasma-enhanced chemical vapor deposition (PECVD) technique to slow down its degradation rate for medical applications. Moreover, the corrosion resistance and mechanical properties of Mg/HA/TiO_2/MgO nanocomposites were enhanced by Si monolayer and Si/ZnO double-layer coatings fabricated using radio frequency magnetron sputtering technique [35]. Silicon (Si), as an essential mineral in human bodies, is substituted alone or in combination with a variety of other materials for filling bone defects [36]. In the early stage of bone calcification, silicon was involved according to the reports of Carlisle [37] and Schwarz and Milne [38]. Moreover, the stimulation of cell proliferation by Mg and Si ionic products was found by Wu and Chang [39]. It has been concluded that Si plays a significant role in bone repair and regeneration of bone. Therefore, the in vivo biological performance of the Mg alloy should be enhanced using a Si-containing coating [40]. In addition, the anticorrosion ability and hemocompatibility of Mg alloy for biomedical application has been significantly improved by MgO coating synthesized using micro-arc oxidation in a multi-step surface modification process. A porous MgO coating as an intermediate layer was prepared on the surface of AZ31 magnesium alloy to improve corrosion resistance [41]. Brink [42] added MgO to a series of bioactive glasses to maintain bioactivity. Some in vitro results actually indicate that MgO has a detrimental effect on apatite formation [43–45]. Furthermore, Oliveira et al. [46] claimed that MgO has a beneficial effect as it improves the early stages of mineralization and contributes to intimate contact with living tissue [14]. Therefore, in the present study, a powder metallurgy technique consisting of ball milling, multi-step cold pressing, and subsequent sintering was used to fabricate of MgO-coated and Si/MgO-coated Mg/HA/TiO_2 nonacomposites for the first time. In addition, microstructure, in vitro biocompatibility, electrochemical, and long-term corrosion behavior of uncoated, MgO-coated and Si/MgO-coated were investigated and have not been performed elsewhere.

2. Materials and Methods

2.1. Preparation of the Powder Samples of Uncoated, MgO-Coated and Si/MgO-Coated Mg/HA/TiO$_2$ Bionanocomposites

Pure magnesium powder (Mg powders, $\geq$99%, 5–20 μm particle size), titanium (IV) oxide (TiO$_2$, anatase nanopowder >99.7%, <100 nm particle size), hydroxyapatite (HA nanopowder $\geq$97%, <100 nm particle size), magnesium oxide powders (MgO $\geq$ 99%, −325 mesh), and silicon powders (Si 99%, −325 mesh) were used as the raw materials. A vacuum drying oven was used to dry the raw material of the nanocomposite and the coating powders (Si powders and MgO with sheet-like morphology) at 220 °C for 10 h. In the next stage, the mixing process by a planetary ball mill was performed on the 77.5 wt % Mg, 12.5 wt % HA, and 10 wt % TiO$_2$ powders in an inert gas atmosphere for 2 h. A uniaxial press at ~840 MPa pressure was used to fabricate cylindrical pellets (Ø10 mm × 5 mm) of uncoated Mg/HA/TiO$_2$ bionanocomposites from the ball-milled powders. Subsequently, the pellets were sintered for 2 h at ~400 °C in a tube furnace under an argon atmosphere to finish the fabrication process of compact specimens. For preparation of MgO-coated, the ball-milled powders of Mg, HA, and TiO$_2$ mixture were pressed at a pressure of ~460 MPa in the first stage of cold pressing. Then, as illustrated in Figure 1, the upper punch exited from the steel die and a specific amount of MgO powders (consisting of sheet-like particles) decanted on the surface of the cold-pressed nanocomposite inside the die. After decanting the MgO powders on the surface of the pressed sample that was inside the steel die, a vibration system was used to homogenize the thickness of the MgO powders in different places on the surface of the pressed nanocomposite.
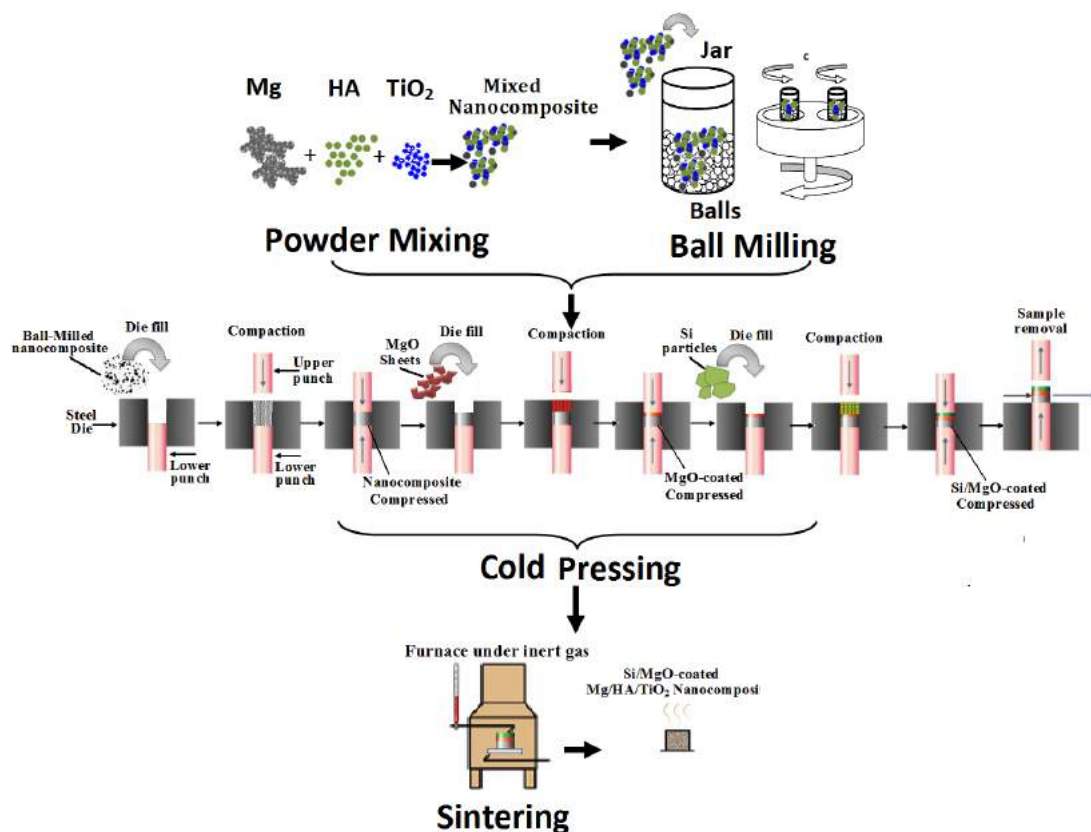

Figure 1. A schematic image of the ball milling-multi step cold pressing-sintering powder metallurgy process to fabricate MgO-coated and Si/MgO-coated Mg/12.5HA/10TiO$_2$ Bionanocomposite.

In the next stage, cold pressing was applied at ~815 MPa to assemble MgO coating on the surface of the Mg/HA/TiO$_2$ nanocomposite. The amount of added MgO in the steel die was determined

by repeating the experiments. Scanning electron microscopy (SEM) observations were made of the thickness of the MgO coating, as well as density measurements and coating adhesion measurements to obtain the acceptable adhesion strength of the fabricated MgO coating layer with the substrate. The minimum required value for the adhesion strength of coatings to the implants is 22 MPa, according to ASTM1147-F [41,47].

In the last stage, the MgO-coated was sintered for 1.5 h at 500 °C under an argon atmosphere. In the case of the double-layer Si/MgO coating, the cold pressing was performed at 340 MPa to press the ball-milled $Mg/HA/TiO_2$ powders and 570 MPa pressure was applied to fabricate the MgO layer on the surface of cold-pressed $Mg/HA/TiO_2$ in the first and second stages of pressing, respectively. In the third step, the specific amount of Si powders decanted on the surface of the MgO-coated into the die, the thickness of Si layer was homogenized at different parts of the surface using a vibration system, and then the powder system was pressed at around 800 MPa of pressure. As reported in the MgO coating process, the amount of Si powder for coating was determined by repeating the coating process to obtain the fabricated coatings with good adhesion strength to the substrate, which is a very important factor to protect Mg-substrate implants against corrosive solutions.

Finally, the Si/MgO-coated was sintered for two hours at 540 °C under an argon atmosphere for densification of the powder sample and better coating adhesion to the substrate. The characterization, corrosion investigations, mechanical analysis, and biological tests were performed on these sintered pellets. The relative density (measured density/theoretical density) of the sintered pellets was considered an important parameter to determine the cold-pressing and sintering conditions, as the minimum ratio of relative density was 85% in order to carry out a reasonable comparison of the corrosion resistance, mechanical characteristics, and cytotoxicity of uncoated and coated $Mg/HA/TiO_2$ bionanocomposites. Table 1 indicates the codified names of the uncoated and coated $Mg/HA/TiO_2$ bionanocomposites.

Table 1. Codified names of uncoated and coated samples.

Full Name of Samples	Codified Name of Samples
Uncoated $Mg/HA/TiO_2$ bionanocomposite	Uncoated nanocomposite
Mono-layered MgO-coated $Mg/HA/TiO_2$ bionanocomposite	MgO-coated
Double-layered Si/MgO-coated $Mg/HA/TiO_2$ bionanocomposite	Si/MgO-coated

2.2. Characterization of the Powder Samples of Uncoated, MgO-Coated and Si/MgO-Coated

The surface and cross-sectional morphologies of the coatings, as well as the corrosion products, were observed using field-emission scanning electron microscopy (FE-SEM, JEOL, Peabody, MA, USA) and transmission electron microscopy (TEM, Philips, Amsterdam, The Netherlands). The crystal structure, phase analysis, and chemical compositions of uncoated, MgO-coated, and Si/MgO-coated and corrosion products were characterized by X-ray diffraction (XRD), energy dispersive X-ray spectroscopy (EDS), and X-ray photoelectron spectroscopy (XPS). Atomic-force microscopy (AFM) was used to investigate the surface morphology and roughness of the uncoated and coated samples. Coating bonding measurements were carried out by a pull-off test using a portable adhesion tester according to standard test method ASTM D4541 [48,49].

2.3. Electrochemical Tests

The electrochemical test was recorded at 37 °C in a glass cell containing 250 mL of Kokubo simulated body fluid (SBF) at a pH ~7.56 using a Versastat3 potentiostat/galvanostat (Princeton Applied Research). Concentrated solutions of NaCl (8.037 g/L), $NaHCO_3$ (0.351 g/L), KCl (0.224 g/L), $K_2HPO_4 \cdot 3H_2O$ (0.231 g/L), $MgCl_2 \cdot 6H_2O$ (0.310 g/L), $CaCl_2$ (0.294 g/L), Na_2SO_4 (0.073 g/L), tris-hydroxymethyl aminomethane $(CH_2OH)_3 CNH_2$ (6.062 g/L) and 1.0 mol/L HCl (40 mL) were used to prepare the SBF solution (known as the Kokubo solution) by pipetting the calculated amounts [13]. The exposed surface area of the tested specimens in the SBF solution was 0.402 cm^2. Moreover,

a saturated calomel electrode (SCE) and a graphite rod were used as the reference electrode and the counter electrode, respectively, where the specimen was the working electrode in a three-electrode cell for the potentiodynamic polarization tests. All of the experiments were recorded at a scan rate of 0.5 mV/s beginning at -250 mV$_{SCE}$ below the open circuit potential. The software allows for the ability to manually control this fitting. A segment of the curve from the E_{corr} (V vs. SCE) was selected for the Tafel fittings, and i_{corr} was subsequently estimated from the value, where the fit intercepted the potential value of the true E_{corr} (V vs. SCE) [50]. All of the potentials referred to the SCE. This machine was also adjusted over a frequency range of 1 Hz to 100 kHz to measure the electrochemical impedance spectra (EIS). The reproducibility of the results was confirmed by repeating each electrochemical test.

2.4. Immersion Tests

The volume of hydrogen gas released from the samples was measured by soaking the samples in SBF solution for 168 h. A sample was immersed in a beaker that was covered with a funnel covering the immersed sample to collect the evolved hydrogen gas in a burette that was fixed above the funnel. Prior to renewing the solution, the volume of the released hydrogen gas was calculated in mL/cm^2, as well as a scaled burette used to measure the hydrogen volume. A benchtop pH-meter was used for measuring the pH of the physiological environment.

2.5. Cell Culture

Cell viability was investigated using the seventh passage of the normal human osteoblasts (NHOst) cells cultured in an osteoblast basal medium (OBM) with the osteoblast growth medium (OGM), which was supplemented with 0.1% ascorbic acid, 10% Fetal Bovine Serum (FBS), and 0.1% of gentamycin. Then, they were placed in an incubator under cell culture conditions (90 $\pm$ 2% humidity, 37 $\pm$ 1 °C, 5% CO$_2$ and 20% O$_2$).

2.6. Cell Viability Testing

An indirect contact method was used to perform the cell viability test using the MTT (3-(4,5-dimethylthiazol-2-yl)-2,5-diphenyltetrazolium bromide) assay. The samples were sterilized in a steam autoclave at 120 °C for 30 min followed by 1 h of ultraviolet (UV) irradiation. Then, the samples were mixed with the OBM media and then kept in an incubator with an atmosphere of 5% CO$_2$ for 72 h at 37 °C. The ratio of the sample surface area to the volume of medium was 1.25 cm^2/mL. After 72 h incubation, a 0.20 μm membrane filter was used to filter the extracted samples. The extracted samples were stored at 4 °C before being used. To perform the MTT assay, 0.15 × 104 NHOst cells were initially seeded in each well of 96-well plates for 24 h, and the media were then replaced with the media containing the extracted samples and then incubated. After 3, 7, and 9 days of incubation, the culture medium was aspirated, 100 μL of fresh medium was added to each well. Then, 10 μL of MTT was added to each well and incubated for 4 h. After incubation, the medium was aspirated, 100 μL of dimethyl sulfoxide (DMSO) was added to each well, and the absorbance was measured at 570 nm (BioTek Eon, BioTek Instruments Inc., Winooski, VT, USA). Cells grown in the typical culture medium and cell-free culture media were used as controls with 100% viability and blank, respectively. For the MTT-assay, triplicates were performed, and the percentage of cell viability was calculated using the formula as Equation (1):

$$\text{Cell Viability } (\%) = \frac{\text{OD}_{sample} - \text{OD}_{blank}}{\text{OD}_{control} - \text{OD}_{blank}} \times 100\% \tag{1}$$

where OD is the optical density [18].

2.7. Cell Adhesion Test

To determine the cell adhesions 12-well culture plates were used to place the sterilized disks (Ø10 mm × 5 mm) of uncoated, MgO-coated and Si/MgO-coated samples then 5.2 × 10^4 osteoblast

cells were seeded in each of the disks. The culture medium was carefully replaced by a fresh one after a three-day interval; however, the detachment of cells should be avoided during the change process of the culture medium. After seven days, the disks of uncoated and coated samples were washed with phosphate buffered saline (1 × PBS, pH 7.46), fixed overnight in 4.2% glutaraldehyde in PBS solution, then subsequent fixation was performed in 1% aqueous osmium tetroxide for one hour. After fixation process, the disks were washed and dehydrated with graded ethanol (40%–100% (*v/v*)). The dehydrated samples were dried by 10 min of soaking in 1:1 and 1:3 (*v/v*) alcohol-hexamethyldisilazane (HMDS) solution and pure hexamethyldisilane (HMDS), respectively. The dried samples were gold coated and the morphology and adhesion of the osteoblast cells were investigated using field-emission scanning electron microscopy.

3. Results and Discussion

3.1. Microstructure, Chemical Composition and Phase Analysis

For an effective comparison, the XRD pattern of the uncoated (Figure 2) nanocomposite substrate is included. This shows the substrate is composed of Mg (PDF#35-0821), HA (PDF#09-0432), and TiO_2 (PDF#21-1272) phases. Figure 2 shows that the MgO-coated mainly consisted of MgO (PDF#45-0946), Mg, and TiO_2.
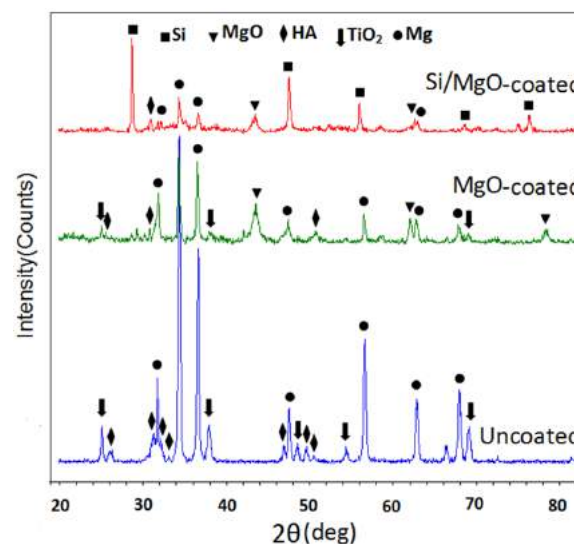

Figure 2. X-ray diffraction (XRD) patterns of the uncoated, MgO-coated and Si/MgO-coated after the milling-cold pressing-sintering process.

The strong Mg and TiO_2 peaks are due to the porous microstructure of the MgO coating; however, the small peaks of HA were almost not detected. With regards to the XRD patterns, the main compound residing on the Si/MgO coating is Si (PDF#27-1402). The intensity of XRD peaks of Mg and TiO_2 are significantly decreased and some of them disappeared because of the thickness of the double-layer coating. To understand the surface chemical composition of uncoated, MgO-coated, and Si/MgO-coated, the outer surface of samples was examined by XPS. It is known that this analysis is used especially for surfaces. Figure 3 shows the overview of the XPS spectra of the uncoated, MgO, and Si/MgO coatings.

As can be seen, O, C, Mg, Ti, Ca, and P elements are detected on the surface of the uncoated Mg/HA/TiO_2 nanocomposite (Figure 3). Ca 2p, P 2p, and O 1s peaks at 352 eV, 138 eV, and 532 eV, respectively, correspond to HA; however, TiO_2 in the nanocomposite substrate is presented by the Ti 2p [51] and O 1s spectra at 458 eV and 532 eV, respectively [51]. The scan analysis of Mg 1s at approximately 1304 eV revealed a peak that may belong to the metallic state of Mg from the

nanocomposite substrate and/or assigned to MgO [11,33,52]. The signal of Mg 2s at ~88.5 eV should come from the magnesium of the nanocomposite substrate [53]. After assembling the porous MgO coating on the nanocomposite surface by the PM route, the intensity of the Ca 2p, P 2p, O 1s, and Ti 2p peaks decreased, whereas the height of Mg 1s and Mg 2p spectra at binding energies (BE) of 50.5 eV and 1304 eV, respectively, are raised, confirming the presence of the MgO layer on the outer surface of the MgO-coated [54,55]. The Si 2p signal assigned to the Si coating [34] is observed at 102 eV in the XPS spectrum of the double-layered coated sample; however, Mg 2s, Mg 1s, Mg 2p, O 1s, Ca 2p, P 2p, and Ti 2p signals due to Mg, MgO, HA, and TiO$_2$ phases weakened remarkably, or even disappeared, which is attributed to the thickness of the Si/MgO coating. The existing of binding energy of the C 1s peak at 286 eV corresponding to the carbon is the result of the preparation process and keeping the sample in air and/or washing it with acetone before conducting the test [34,55]. Mg 1s at approximately 1304 eV may be assigned to the surface magnesium existing in the form of the oxidized state, indicating the formation of MgO [11,52]. There is no other visible contribution of metallic magnesium related to the main Mg KLL emission peaks. These spectra that were found in the range 304.4–308.8 eV are attributed to the oxidation of polycrystalline Mg [56]. FE-SEM images in Figure 4 show the surface morphologies of the bare sample and the coatings that were assembled by the PM technique. As can be seen (Figure 4a), the large particles with plate-like morphology that are uniformly distributed in the substrate of the bare nanocomposite are surrounded by fine powders. The surface microstructure of the MgO-coated is homogenous and porous, comprising the sheet-like particles (Figure 4b,c). However, the FE-SEM micrographs depict a relatively dense and rough layer consisting of irregular-shaped particles of micron size covering the outer surface of the Si/MgO-coated, whereas some porosities are observed on the coating (Figure 4d,e). X-ray elemental mapping indicates the Mg particles appear with two types of morphology: some of the Mg particles have a plate-like morphology, whereas the remainder of the Mg, accompanied by O, Ca, P, and Ti as fine particles, is distributed homogenously among the plates within the powder system of the Mg/HA/TiO$_2$ nanocomposite.
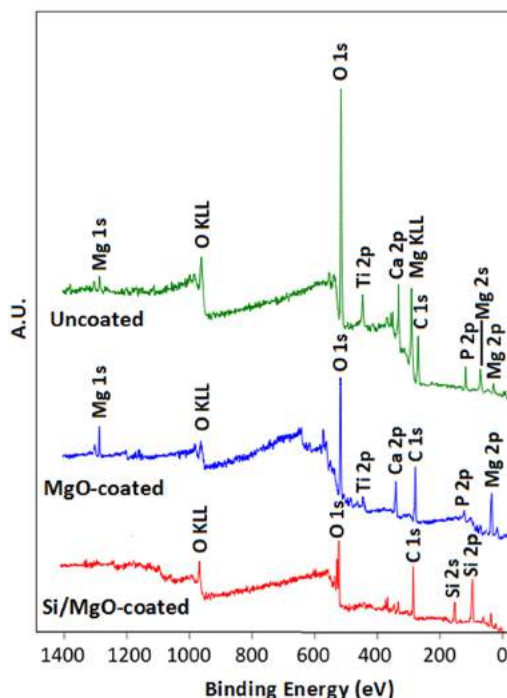

Figure 3. Survey X-ray photoelectron spectroscopy (XPS) spectra of the uncoated, MgO-coated and Si/MgO-coated after the milling-pressing-sintering process.
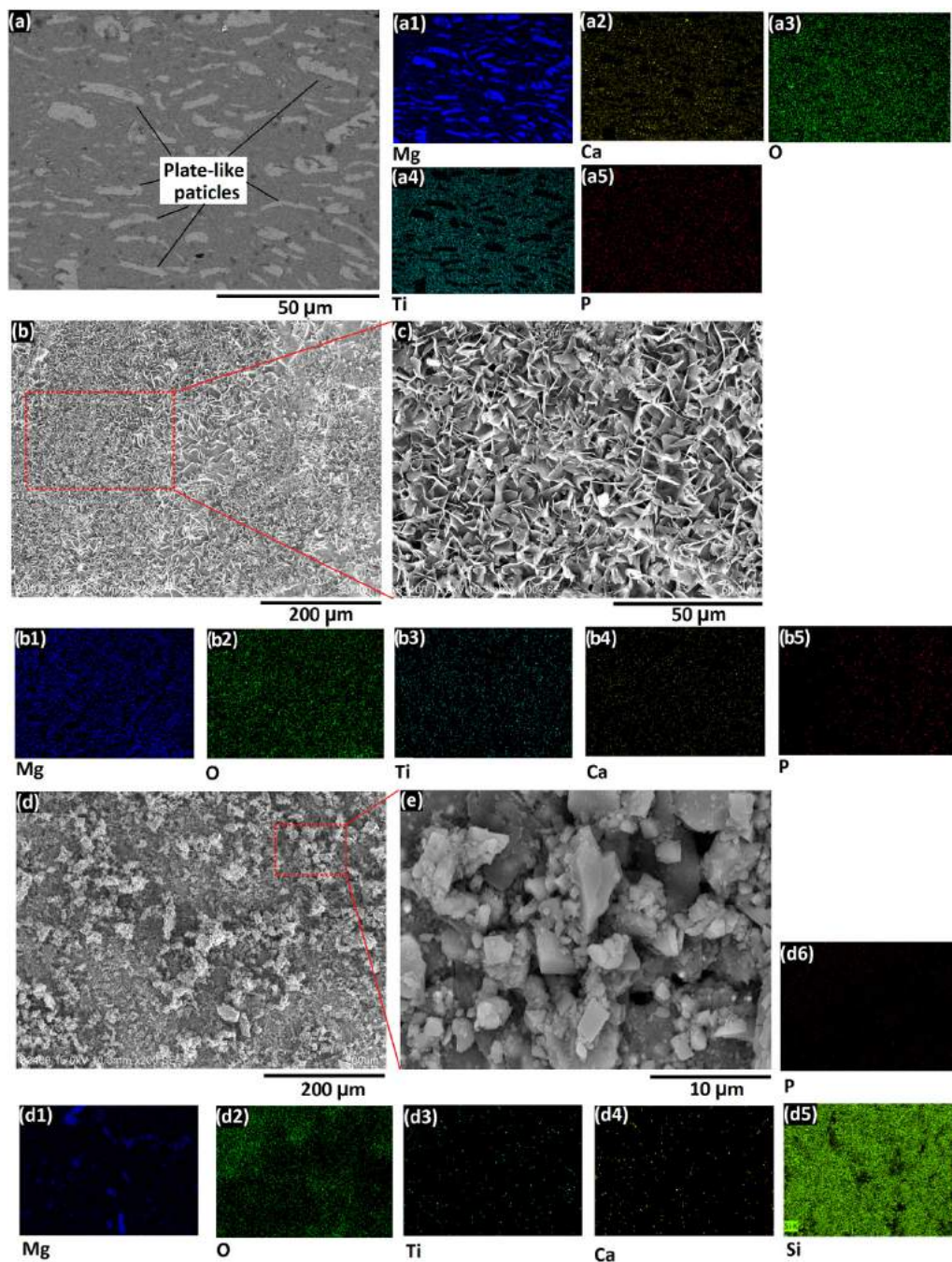
Figure 4. Surface field-emission scanning electron microscopy (FE-SEM) micrographs of (**a**) uncoated; (**b**,**c**) MgO-coated and (**d**,**e**) Si/MgO-coated. X-ray elemental mapping of surfaces of (**a1**–**a5**) uncoated, (**b1**–**b5**) MgO-coated and (**d1**–**d6**) Si/MgO-coated.

With regards to the elemental mapping images, the distribution of elements on the surface of coated samples confirms the fabrication of MgO and Si on the outer surfaces of the MgO-coated and Si/MgO-coated, respectively. The AFM images (Figure 5) show the surface morphology and roughness of some selected areas on the surface of uncoated and coated samples. The sheet-like morphology of MgO particles, as well as the irregular shape of Si particles, can be confirmed using AFM images; however, the surface of the uncoated sample is smooth. The average roughness value of surface increased from 187.2 nm on the bare nanocomposite, to 724.6 nm and 935.5 nm for MgO-coated and Si/MgO-coated, respectively.
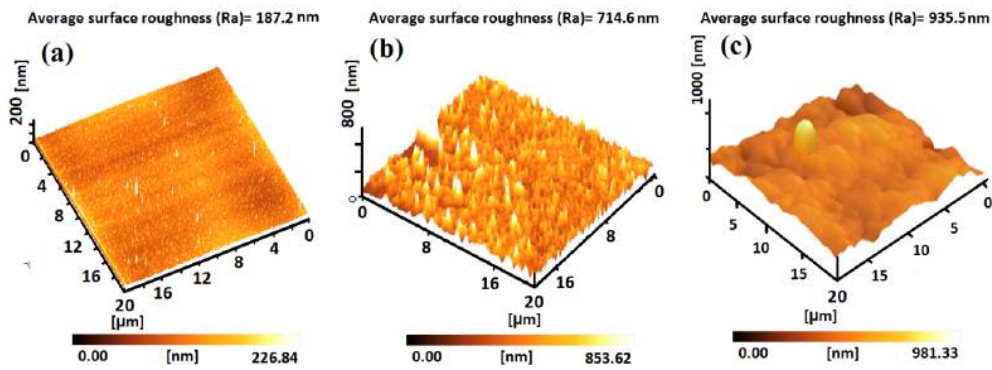
Figure 5. 3D-atomic-force microscopy (AFM) image of (**a**) uncoated, (**b**) MgO-coated and (**c**) Si/MgO-coated samples after the ball milling-cold pressing-sintering process.

Figure 6 presents the cross-sectional images of the mono- and double-layered coatings. The MgO-coated with an average thickness of 38 μm composed of MgO sheets is porous without any discontinuity in the interface between the coating and the substrate. However, the double-layer coating consisting of an inner layer of sheet-like particles with well-dispersed porosities, as well as the Si particles with irregular shape, formed the densely-packed outer layer on the surface of the Si/MgO-coated. The average coating thickness of the Si/MgO achieved 57 μm: The thickness of the inner layer is around 36 μm; however, the average thickness of the outer coverage is estimated at 20 μm. The morphology and thickness of the coatings showed a fair degree of uniformity; moreover, the adhesion of the coatings to the substrate is also confirmed by the cross-sectional micrographs. Furthermore, the X-ray elemental mapping of the double-layer Si/MgO coating (Figure 6k,l,m related to Figure 6h) confirm the fabrication and thickness uniformity of coatings as Si is shown in green in the outer layer of the coating, whereas Mg and O on the inner side of the coating are illustrated by blue and red, respectively.

The TEM images depict the morphology of MgO sheets and irregularly-shaped particles of Si accompanied with their EDS analysis (Figure 6a–d). The TEM-EDX pattern exhibits only the presence of Mg and O elemental compositions, ensuring the chemical purity of the MgO sheet-like powders. In order to evaluate the bonding strength of the mono- and double-layer coatings, the pull-off test was performed on the coated samples. The bonding strength of the monolayer MgO coating to the substrate is measured as 35.6 ± 1.2 MPa, whereas by fabricating Si as a second coating layer the bonding strength of the whole double-layer Si/MgO coating to the substrate decreased to 31.4 ± 2.7 MPa. This might have happened as a result of increasing the thickness of the coating, as more particles agglomerate on the outer surface of the coating and/or show less uniformity, as well as the increasing roughness of the Si/MgO coating compared to the monolayer MgO.
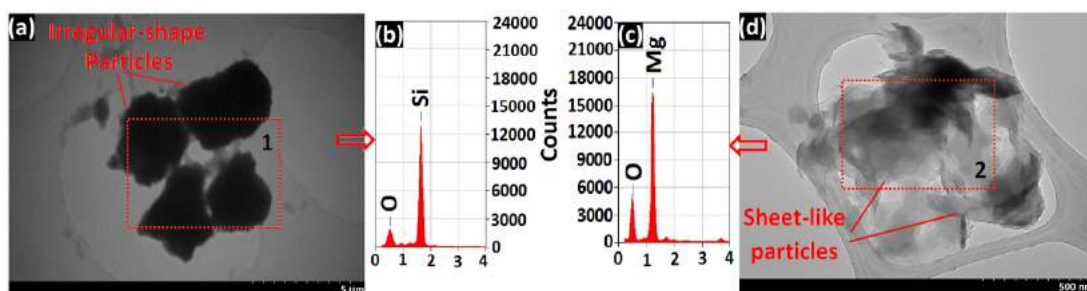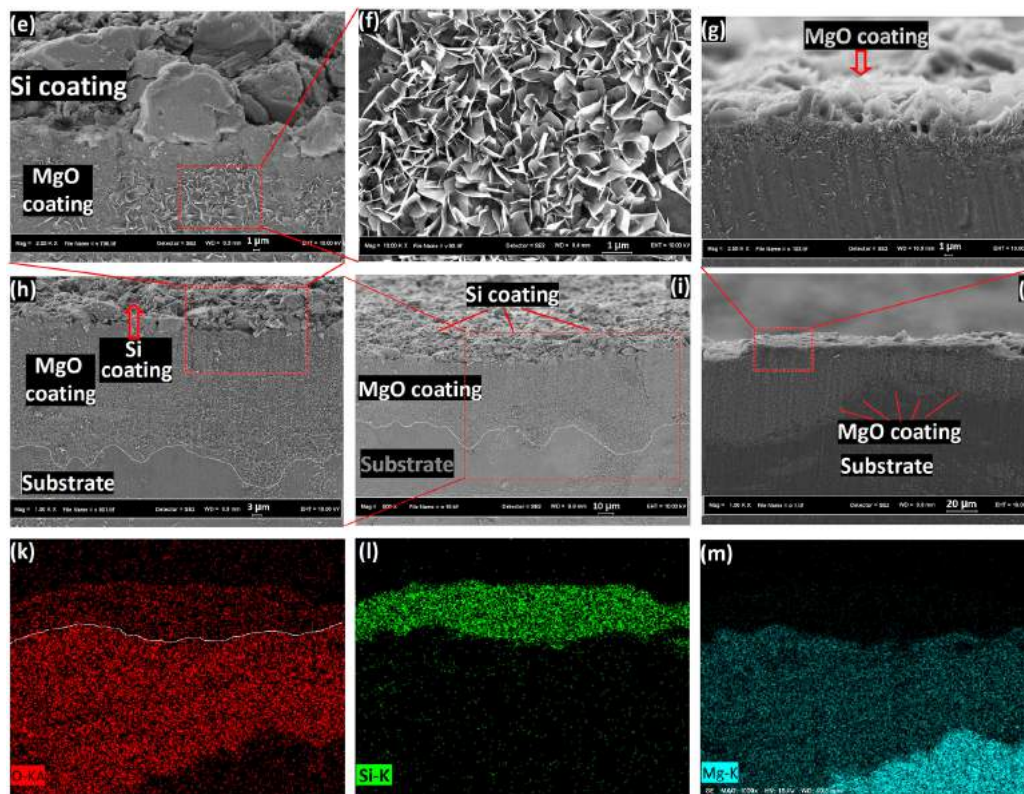

Figure 6. *Cont.*

Figure 6. Transmission electron microscopy (TEM) images (**a**) Si particles, (**d**) MgO sheets, energy dispersive X-ray spectroscopy (EDS) analyses (**b**) area 1 and (**c**) area 2. Cross-sectional FE-SEM micrographs of (**e,f,h,i**) Si/MgO-coated, (**g,j**) MgO-coated and (**k,l,m**) X-ray elemental mapping of Figure 5h.

3.2. Electrochemical Corrosion Tests

The ability of a coating to protect the substrate can be evaluated by electrochemical impedance spectroscopy (EIS). Figure 7 shows the Nyquist plots (Figure 7a) and the Bode plots (Figure 7b,c) for the bare, MgO-coated, and Si/MgO-coated in SBF solution. The differences in the diameter size of capacitive Nyquist loops for uncoated and coated samples can be attributed to the charge transfer resistance of the corrosion process (Figure 7a). This discloses that the Si/MgO-coated presents the overall largest constant loop among all the samples. The diameter of the capacitive loop indicates the anticorrosion property [57,58], evidencing that the Si/MgO coating provides a more effective barrier effect against corrosive solution. According to the used models illustrated in Figure 7d, the spectrum of the sample without coating could be fitted using the simplified equivalent electrical circuit (EEC) with one R_2–CPE_2 circuit (Figure 7d), where R_2 is the charge transfer resistance, CPE_2 is the double-layer capacitance, and R_S represents the solution resistance. In the allocated circuit of MgO coated, the R_1–CPE_1 elements describe the MgO coating, as well as the R_2–CPE_2 elements which are related to the substrate. Meanwhile, the monolayer MgO increased the diameter of the capacitive loop, indicating that the MgO coating in the SBF electrolyte can improve the anticorrosive properties of the nanocomposite. The quantitative parameters of the EEC elements, which characterize the coverage layers of MgO and Si (formed as a result of the powder metallurgy route) were calculated by fitting the experimental impedance spectra using EEC with three R–CPE-circuits (Figure 7d). The emergence of the third time constant (R_3–CPE_3) is related to the MgO intermediate layer.
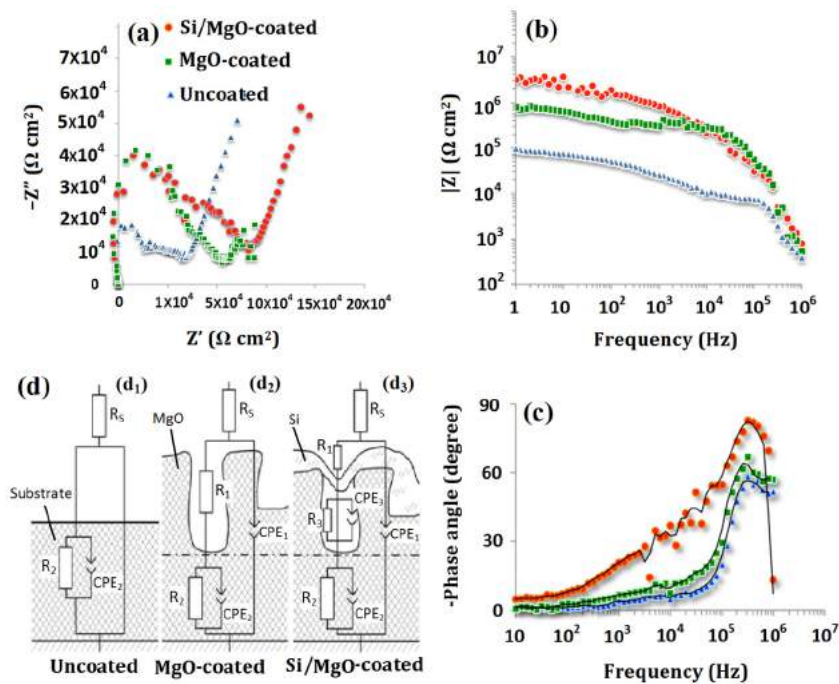
Figure 7. (**a**) Nyquist plots, Bode plots (**b**) impedance modulus vs. frequency plots and (**c**) phase angle vs. frequency plots for the uncoated, MgO-coated, and Si/MgO-coated in SBF solution; (**d**) The models for the coatings structure and the appropriate equivalent electrical circuits, used for experimental impedance data fitting ((**d$_1$**) with one *R–CPE* circuit, (**d$_2$**) with two *R–CPE* circuits and (**d$_3$**) with three *R–CPE* circuits).

The presented three-*R–CPE*-circuit EES describes the Si/MgO-coated under examination. The electrochemical resistance (R_e), regarded as a measure of corrosion resistance, is calculated by adding R_1, R_2, and R_3. The R_e values of the MgO-coated and the Si/MgO-coated are larger than that of the uncoated nanocomposite, which indicates the protection of the two kinds of coatings for the substrate. The R_e of the MgO-coated (57.9 kΩ·cm^2) was nearly five orders of magnitude larger than that of the uncoated sample (11.6 kΩ·cm^2). Furthermore, the value of electrochemical resistance of the Si/MgO-coated (R_e = 82.6 kΩ·cm^2) measured close to eight orders of magnitude higher than that of the uncoated sample. As can be seen in Figure 7a, the diffusion control mechanism of Warburg impedance is indicated by the emergence of a tail in the Nyquist plots of the samples. When the counter-ions move through the surface, the Warburg behavior takes place, which indicates the slower occurrence of the diffusion process than the metal charge-transfer reaction and, as a result, a diffusion barrier mechanism is developed on the surface against the corrosive attack [59–61]. As shown in the Bode plots (Figure 7b), in the low-frequency region, the initial modulus values for MgO-coated and Si/MgO-coated are higher than that of the uncoated sample. The resistance is revealed by the charge transfer-controlled process at high frequency, while the mass diffusion-controlled reactions dominated at a low frequency in the Bode plots. The higher impedance difference between the high and the low frequency means that better corrosion resistance is provided [57]. Furthermore, the Si/MgO-coated possessed the highest impedance modulus, compared with the uncoated and MgO-coated. This speculation is clearly reflected by the lower phase angle of Si/MgO (81°) compared to only the MgO coating (67°) and the bare (53°) sample. For the Si/MgO-coated, the curves of the Bode plots (Figure 7c) reveal the time constants (the peak at the minimum degree of phase angle) at frequencies of 39,810 Hz, 31,622 Hz, and 25,188 Hz for Si/MgO-coated, MgO-coated, and uncoated samples, respectively. The presence of the time constant at a higher frequency and lower phase angle is attributed to the Si/MgO coating property, suggesting it possesses a fine physical barrier to the corrosive media. As a comparison, MgO-coated illustrates a similar curve shape to that of the bare

nanocomposite. This means that corrosion has the same process on the bare substrate and on the MgO-coated surface; however, the corrosion resistance is different. The EIS electrochemical parameters of the uncoated and coated samples are indicated in Table 2. The results of the Nyquist diagram are consistent with those obtained through the Bode diagram and are also supported by the plot of the phase angle and impedance versus frequency.

Table 2. Fitted electrochemical impedance spectroscopy (EIS) results of uncoated, MgO-coated and Si/MgO-coated in simulated body fluid (SBF) solution.

EIS Parameters\Samples	Uncoated	MgO-Coated	Si/MgO-Coated
R_e (kΩ·cm^2)	11.6	57.9	82.6
Phase angle (°)	53	67	81
Frequency (Hz)	25,188	31,622	39,810

The corrosion behaviors of MgO-coated, Si/MgO-coated, and uncoated samples were evaluated by potentiodynamic polarization tests. Figure 8 shows the potentiodynamic polarization curves of different samples in SBF aqueous solution.
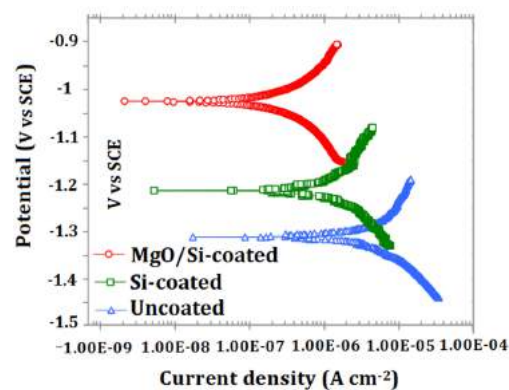

Figure 8. Potentiodynamic polarization curves of uncoated, MgO-coated and Si/MgO-coated in simulated body fluid (SBF) solution.

For magnesium and its alloys, the cathodic polarization curve generally represents the cathodic hydrogen evolution by water reduction, and the anodic polarization is considered to represent the dissolution of magnesium or corrosion behaviors of the surface protective layer. The anodic and cathodic reactions can be written as follows:

$$Mg \rightarrow Mg^{2+} + 2e^{-} \text{ Anodic reaction} \tag{2}$$

$$2H_2O + 2e^{-} \rightarrow H_2 + 2OH^{-} \text{ Cathodic reaction} \tag{3}$$
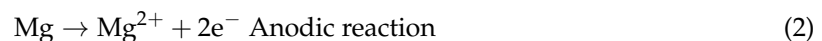
The corrosion potentials E_{corr} and corrosion current density i_{corr} were calculated by the Tafel method through linear extrapolation of the cathodic polarization zone [62]. The corrosion current density (i_{corr}), corrosion potential (E_{corr}, V_{SCE}), cathodic Tafel slopes (β_c), anodic Tafel slopes (β_a), and corresponding corrosion resistance (R_P) of the specimens extracted from the polarization curves are listed in Table 3.

As can be observed in Figure 8 and Table 3, lower corrosion current densities were obtained for the coated samples than for that of the uncoated sample. Additionally, the polarization resistance (R_P) of the bare and coated samples can be calculated using the electrochemical parameters (i_{corr}, β_a, and β_c) Tafel plots in Equation (4) as follows [19,63,64]:

$$R_P = \frac{\beta_a \, \beta_c}{2.3 \, (\beta_a + \beta_c) i_{corr}} \tag{4}$$

The corrosion current density of the sample coated by MgO (2.8 μA/cm^2) is lower compared to the case of the bare sample (5.3 μA/cm^2), indicating the MgO coating significantly decreased the corrosion rate of the nanocomposite. It is evident that the corrosion current density (i_{corr}) decreased gradually from 2.8 μA in the MgO-coated to 0.89 μA for the Si/MgO-coated sample. The Si/MgO-coated shows the highest corrosion resistance (67.36 kΩ·cm^2) among the uncoated (12.17 kΩ·cm^2) and MgO-coated (21.28 kΩ·cm^2). The Si/MgO coating underwent the lowest i_{corr}, which might be due to its microstructure, thickness, and/or chemical composition. This implies that the Si/MgO coating effectively suppresses the corrosion process. In addition, another important finding from the polarization curves is the corrosion potential (E_{corr}) that MgO and Si/MgO coatings led to an increase in its value in the SBF solution. As shown in Table 1, the Si/MgO-coated depicts the most positive E_{corr} compared with the bare and MgO-coated. The more positive value of E_{corr} was obtained for the MgO layer that formed by PM method on the surface of uncoated sample compared with the E_{corr} of uncoated nanocomposite. The more positive E_{corr} means the sample is more stable thermodynamically against corrosion, meanwhile, the lower i_{corr} means a slower corrosion process kinetically [65].

Table 3. Electrochemical parameters of the uncoated and MgO- and Si/MgO-coated Mg/HA/TiO$_2$ nanocomposites in SBF solution obtained from the polarization test.

Sample	Corrosion potential, E_{corr} (mV vs. SCE)	Current Density, i_{corr} (μA/cm^2)	Cathodic Slope, β$_c$ (mV/Decade) vs. SCE	Anodic Slope, β$_a$ (mV/Decade) vs. SCE	Polarization Resistance, R_P (kΩ·cm^2)
Uncoated	−1315.6	5.3	279.4	316.8	12.17
MgO-coated	−1208.8	2.8	232.7	347.2	22.86
MgO/Si-coated	−1023.7	0.89	205.8	410.6	69.04

3.3. Immersion Tests

Immersion tests were undertaken to evaluate the long-term corrosion mechanism of the Si/MgO-coated, MgO-coated and uncoated nanocomposites. The long-term in vitro degradation behavior of samples was examined to measure hydrogen evolution during the immersion of samples in SBF solution for different times. Hydrogen evolution is usually measured as an indicator of the magnesium degradation rate [18]. It is well known that the overall corrosion reaction of magnesium in aqueous solution at its corrosion potential can be expressed as follows:

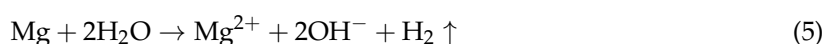$$Mg + 2H_2O \rightarrow Mg^{2+} + 2OH^- + H_2 \uparrow \tag{5}$$

Figure 9 depicts the cumulative hydrogen gas evolution plots illustrated for the uncoated, MgO-coated, and Si/MgO-coated. The cumulative hydrogen amount released from the bare sample is higher compared with that of the MgO and Si/MgO coatings. During the immersion, the lowest hydrogen evolution amount was measured for the Si/MgO-coated. This described the fact that the uncoated and MgO-coated underwent more severe corrosion in SBF. However, the dual-layered Si/MgO coating could effectively inhibit the degradation of the uncoated sample. In addition, it can be observed that the hydrogen evolution rate amplified after 120 h from 22.5 mL/cm^2 in the uncoated sample to 15 mL/cm^2 for the MgO-coated, respectively. The results indicate that the Si/MgO coating remarkably suppressed hydrogen evolution (10.5 mL/cm^2) over the long immersion period, considerably lower compared to all other samples.

3.4. Characterization and Microstructure of Immersed Samples in SBF Solution

After seven days of immersion in the SBF solution, in vitro degradation and mineralization on the surfaces of uncoated, MgO-coated, and Si/MgO-coated were evaluated using XRD, XPS, and microstructural investigations. In order to identify the phases of the corrosion products, XRD was conducted on the surface of the uncoated and coated samples after immersion in SBF for seven days, as shown in Figure 10.
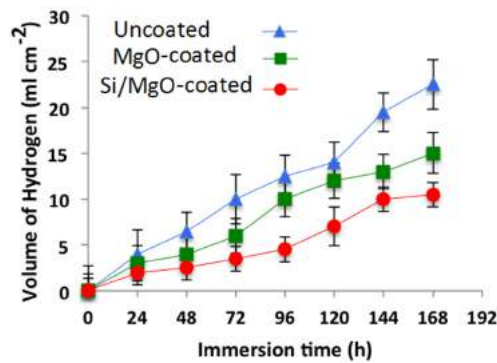
Figure 9. Hydrogen evolution during immersion of uncoated, MgO-coated and Si/MgO-coated in SBF solution for duration of 168 h.
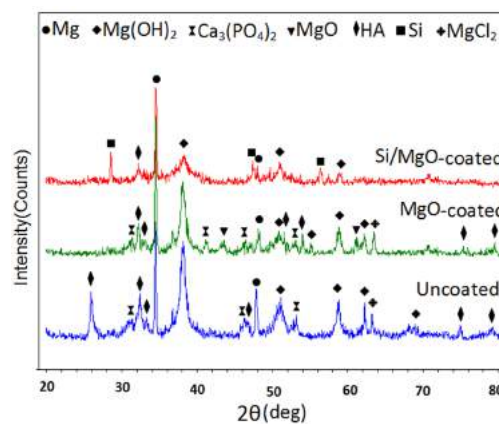

Figure 10. XRD patterns of uncoated, MgO-coated and Si/MgO-coated after 168 h of immersion in an SBF solution at 37 °C.
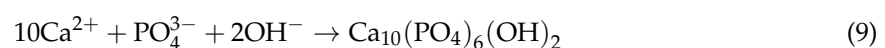
It can be found that Mg, $Mg(OH)_2$, HA, $Ca_3(PO_4)_2$, and $MgCl_2$ phases were detected on the surface of the uncoated immersed sample. The formation of apatite illustrated the bioactivity of the coating [12,13]. It is well known that the overall corrosion reaction of magnesium in aqueous solution as its corrosion potential can be expressed by the anodic reaction ($Mg \rightarrow Mg^{2+} + 2e^-$) and cathodic reaction ($2H_2O + 2e^- \rightarrow H_2\uparrow + 2OH^-$). Thus, $Mg(OH)_2$ precipitated in the initial stage of degradation of the Mg-based nanocomposite substrate according to the following reaction:

$$Mg^{2+} + 2OH^- \rightarrow Mg(OH)_2 \text{ (product formation)} \tag{6}$$
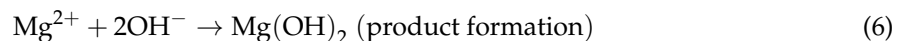
By increasing the immersion time, the chloride ions (Cl^-) of the SBF solution would react with $Mg(OH)_2$ to form a more resoluble $MgCl_2$ phase based on Equation (7) [66]:

$$Mg(OH)_2 + 2Cl^- \rightarrow MgCl_2 + 2OH^- \tag{7}$$

CaP compounds, such as HA and $Ca_3(PO_4)_2$ formed on the surface of the immersed samples due to the reaction of the phosphate ions (HPO_4^{2-} or PO_4^{3-}) and Ca^{2+} with OH^- ions in the SBF solution based on the phase transformations of Equations (8)–(10) as follows:

$$10Ca^{2+} + 8OH^- + 6HPO_4^{2-} \rightarrow Ca_{10}(PO_4)_6(OH)_2 + 6H_2O \tag{8}$$

$$10Ca^{2+} + PO_4^{3-} + 2OH^- \rightarrow Ca_{10}(PO_4)_6(OH)_2 \tag{9}$$

$$3Ca^{2+} + 2PO_4^{3-} \rightarrow Ca_3(PO_4)_2 \tag{10}$$

XRD peaks of MgO are detected in X-ray patterns of corrosion products of the MgO-coated sample; moreover, despite the better corrosion resistance of the MgO-coated than that of the bare sample, the strong peaks of Mg(OH)$_2$ are detected, which can be related to the presence of the MgO layer on the outer surface of sample and, as a result, formation of Mg(OH)$_2$ according to Equation (11):

$$MgO + 2H_2O \rightarrow Mg(OH)_2 \tag{11}$$

However, a significant decrease in intensity of the allocated XRD peaks of corrosion products, such as Mg(OH)$_2$ and CaP components, was observed for the Si/MgO-coated after seven days of immersion in SBF. Furthermore, the XRD spectra of the substrate phases, such as Mg, HA, and TiO$_2$ of Mg/HA/TiO$_2$, as well as coating components (MgO and Si peaks), weaken remarkably, and even disappear, demonstrating the deposition of the corrosion products on the surface of the immersed Si/MgO-coated. It can be described by the precipitation of amorphous phases after immersion in SBF. FE-SEM images depicting uncoated nanocomposite immersed in SBF solution suffers more serious corrosion attack and larger cracks than the coated samples (Figure 11).
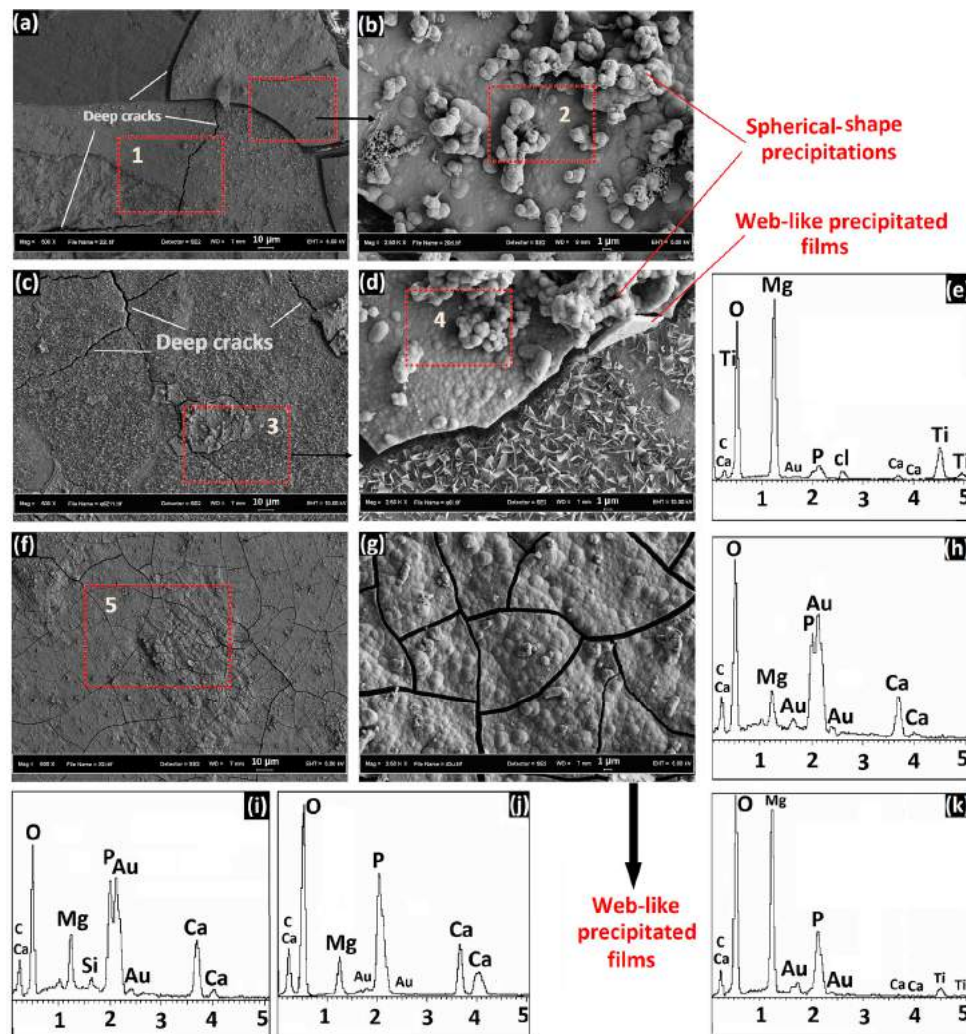

Figure 11. Surface FE-SEM images of (**a**,**b**) uncoated (**c**,**d**) MgO-coated; (**f**,**g**) Si/MgO coated and EDS analysis (**e**) area 1, (**h**) area 2, (**k**) area 3, (**j**) area 4 and (**i**) area 5 after 7 days of immersion in an SBF solution at 37 °C.

However, after seven days of immersion in SBF, the large and deep cracks were almost not detected on the surface of the Si/MgO-coated. Additionally, relatively slight corrosion attack and only some uniform narrow corrosion cracks are observed. It was strongly proved by the FE-SEM images that the Si/MgO coating can significantly enhance the anti-corrosion property of the Mg-based nanocomposite substrate. Moreover, some deep and large cracks appeared on the surface of the MgO-coated, indicating that due to the numerous numbers of pores in the MgO coating, this single-layer coating alone is not sufficient to protect the corrosion of Mg-based nanocomposites for a long period. Hence, the improvement and sealing of the MgO coating by an extra coverage is required. As can be seen, the deposited corrosion products on the bare nanocomposite can be roughly divided into two regions, the interface region and the outer region. The outer part comprises deposited films that cluster with a spherical shape, randomly scattered on the surface of these films. Based on the EDS analysis, Ca and P increased rapidly in the outer region, whereas magnesium decreased significantly (Figure 11h), indicating these films are CaP components. However, the elemental composition of the interface region of the corroded surface was mainly composed of Mg and O (Figure 11e), demonstrating the presence of $Mg(OH)_2$ by comparison of the EDS results with X-ray patterns of the corrosion products. After seven days of immersion, the main part of the surface of the MgO-coated was covered by sheet-like particles and fine powders. Mg, O, P, Ca, and Cl were found on area 3 (Figure 11k) while the contents of Mg and O are all maintained at higher levels than those of the bare nanocomposite. This shows the presence of MgO and $Mg(OH)_2$ phases among the corrosion products of the MgO-coated by adapting EDS analysis with XRD results. Calcium and phosphorus are also detected in area 3 (Figure 11k), indicating electrolyte components can reach the inner part of the MgO coating and finally be absorbed into the substrate. Ca, P, and O, which precipitated from the SBF solution, are detected as the main elements of web-shaped films; additionally, a number of spherical particles were deposited on the surface of these films by immersion in SBF (area 4). By considering EDS and XRD, the web-like films accompanied with the spherical-shape precipitation are shown to be composed of CaP components. The ability to form the apatite on the implant surface in simulated body fluid is considered as an indication of osteointegration capability [67]. The content of Ca and P in the MgO coating is higher than that of the bare sample, indicating better mineralization performance [68]. For the Si/MgO-coated, there is marked difference in the surface morphology after seven days of immersion in comparison with the uncoated and MgO-coated. With regard to the Figure 11f,g, web-shaped films covered the whole surface of Si/MgO-coated. Based on the EDS elemental analysis (Figure 11i), this film is mainly composed of Ca, P, and O, which indicates the deposition of CaP compounds on the surface of the Si/MgO coating after seven days of immersion in the SBF solution (area 5). On the other hand, the XRD peaks of CaP compounds were not detected among the X-ray patterns of the corrosion products precipitated on the surface of the Si/MgO-coated. This may have resulted for two reasons: first, the thickness of the web-shaped film is less than that required for detection by XRD; and, second, these films comprising CaP compounds could be amorphous. The Au peaks appeared because of the gold coating needed to prepare the samples for FE-SEM investigations. The chemical composition of the products of corrosion precipitated on the samples soaked for seven days in SBF was determined using XPS analysis (Figure 12). The characteristic binding energies of Mg, O, Ca, P, Ti, and C elements were revealed in the XPS survey scan spectra of immersed bare samples. The presence of carbonates on the surface of the immersed sample due to inadvertent contamination is indicted by the C 1s peak at ~286 eV [55]. The Ti 2p peak at a binding energy of ~458.8 eV corresponded to the presence of TiO_2 [51] within the substrate of samples. The scan analysis of Mg 1s at approximately 1304 eV revealing one peak belonging to metallic Mg and/or MgO [52]. The Ca 2p and P 2p peaks resulted from the deposition of calcium phosphate components on the samples immersed for seven days.

High-resolution X-ray photoelectron spectroscopy performed for the Ca 2p and P 2p peaks to determine the detailed chemical composition of CaP components deposited on the samples during the immersion in SBF solution (Figure 13). As illustrated in Figure 13, the precipitation of HA is indicated

by the Ca 2p1/2 peaks appearing at ~347.1 eV; however, the Ca 2p3/2 peaks at ~346.4 eV present the deposition of the $Ca_3(PO_4)_2$ phase [23]. The P 2p spectrum consisted of three peaks (Figure 13), which included the P 2p1/2 peak at ~133.2 eV and the P 2p3/2 peak at ~132.6 eV for $Ca_3(PO_4)_2$ and HA, respectively [69]. The Ca 2p and P 2p peaks revealed at ~345.2 eV and ~131.4 eV, respectively, are attributed to the formation of amorphous calcium phosphate components during the soaking process in SBF (Figure 13) [23].
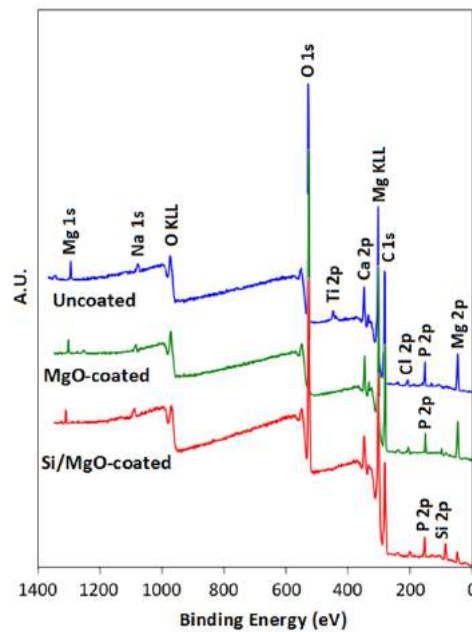

Figure 12. Survey XPS spectra of the uncoated, MgO-coated and Si/MgO-coated after 7 days of immersion in an SBF solution at 37 °C.
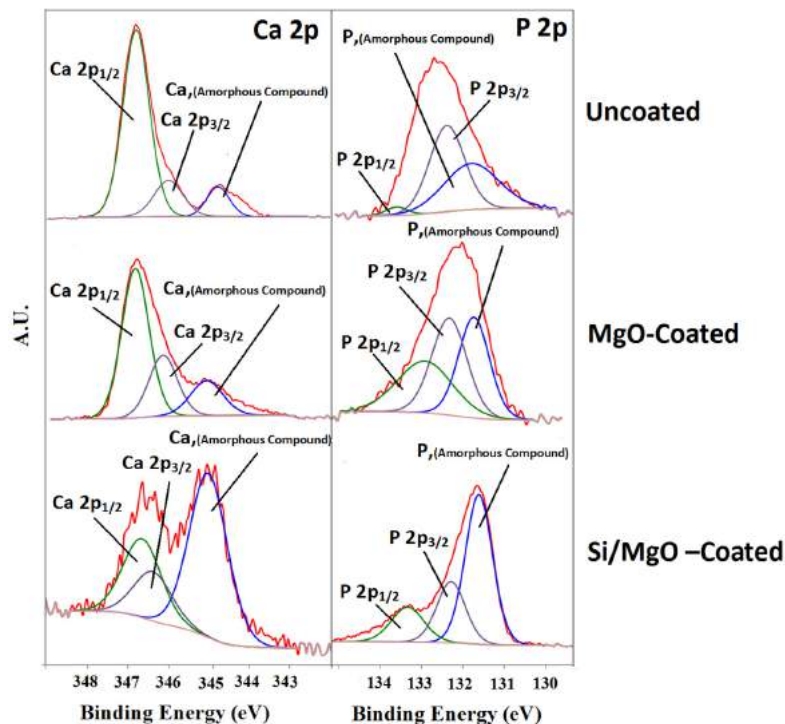

Figure 13. Detailed XPS spectra of the P 2p and Ca 2p peaks of uncoated, MgO-coated and Si/MgO-coated after 7 days of immersion in a SBF solution at 37 °C.

With regard to the intensity of high-resolution X-ray photoelectron Ca 2p and P 2p spectra, a greater amount of $Ca_3(PO_4)_2$ precipitation was detected on the coated samples than that of the uncoated sample after seven days of immersion in the physiological solution, whereas the deposition of HA on the coated nanocomposites was reduced by the restricted contact area between the substrate of the nanocomposite comprising of HA and SBF solution due to the fabrication of the coatings. The HA particles in the substrate can act as places to form and grow new HA precipitation during immersion. After seven days of immersion in the SBF solution, the intensity of the related spectra to the amorphous CaP components increased in the corrosion products of the coated samples compared to those of the uncoated nanocomposite (Figure 13). Furthermore, the O 1s spectrum at ~531 eV can arise due to hydroxyl ($-OH$), carbonate $(CO_3)^{2-}$, and/or phosphate (PO_4^{3-}) groups [70,71]. The presence of magnesium hydroxide among the corrosion products was demonstrated by a single Mg 2p peak (Figure 12) at a binding energy of 50.5 ± 0.1 eV (BE) [72,73]. As can be indicated by the decreased intensity of the Mg 2p spectra, a lesser amount of magnesium hydroxide precipitated on the Si/MgO-coated compared to those of the uncoated and MgO-coated immersed specimen samples, which indicate enhanced degradation resistance of the $Mg/HA/TiO_2$ bionanocomposite with the Si/MgO coating.

The existence of Cl^- and Na^+ ions in the physiological environment resulted in the appearance of Cl 2p and Na 1s peaks among the XPS spectra of samples immersed for seven days in SBF solution [72]. According to the EDS and XPS results, the amorphous components are CaP. A closer look at the morphology and microstructure of the corrosion products that were precipitated on the bare and coated nanocomposites with seven days of immersion in the SBF solution were obtained under TEM, and are presented in Figure 14.
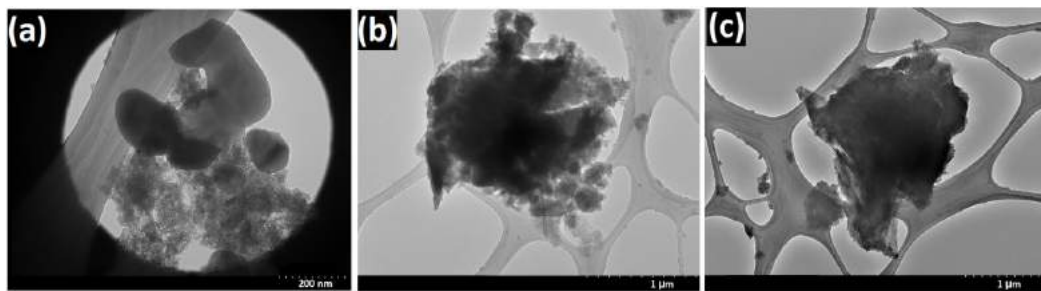

Figure 14. TEM micrographs of corrosion products for (**a**) uncoated; (**b**) MgO-coated and (**c**) Si/MgO-coated after 7 days of immersion in a SBF solution at 37 °C.

The presence of spherically-shape particles with a particle size of approximately 200 nm, accompanied with the agglomerates precipitated on the immersed uncoated sample detected by the FE-SEM observations, is confirmed by TEM analysis (Figure 14a). As indicated in Figure 14b, the corrosion products deposited on the MgO-coated sample are composed of agglomerates, fine powders, spherically-shaped and sheet-like particles; however, the presence the films with irregular shape in corrosion products of Si/MgO-coated sample was demonstrated by TEM observations (Figure 14c).

3.5. Cell Viability, and Attachment of NHOst Osteoblasts

In fact, the ideal biodegradable candidate should have a suitable degradation rate to allow the implant to maintain mechanical support during tissue healing while being nontoxic and compatible with cells [52,74,75]. The relative cell viability (% of control) of the osteoblast cells (NHOst) was determined after three, seven, and nine days indirect treatment with uncoated, MgO-coated, and Si/MgO-coated by extraction media using MTT assay (Figure 15). The data are presented as mean $\pm$ SD and values with $p < 0.05$ were considered as statistically non-significant. The percentages of cell viability were calculated from the obtained OD using the reported Formula (1) for further comparison. After three days of incubation, the viability of the NHOst cells cultured in the

extraction medium of the Si/MgO-coated is $75 \pm 3\%$. However, the extracted medium of the uncoated nanocomposite shows significantly reduced cell viability and was determined to be $61 \pm 6\%$. The NHOst cells after incubation with the MgO-coated extraction medium for three days display less cell viability ($67 \pm 2\%$) compared to that of the Si/MgO-coated. In the first three days of incubation, the high cytotoxicity of the uncoated sample to the NHOst osteoblasts was indicated by the cell viability percentages. However, in comparison with the uncoated nanocomposite, the MgO-coated shows better biocompatibility. Additionally, pH values of the extracted media were monitored every 24 h for possible changes. The pH values of the cell-free culture media collected from uncoated nanocomposite after three, seven, and nine days were 8.1, 8.6, and 8.9, respectively. The values for the MgO-coated are 7.5, 7.8, and 8.2, and for the Si/MgO-coated are 7.4, 7.6, and 7.7, respectively, whereas the pH value of the culture medium (without the bare sample) remained unchanged (pH = 7.3).
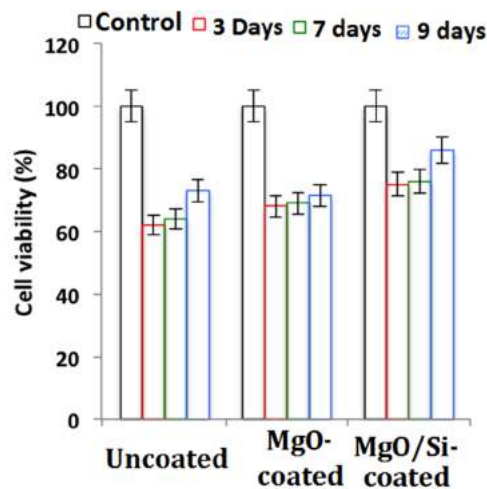

Figure 15. Normal human osteoblast (NHOst) viability cells results indicated by MTT assay after indirect treatment with uncoated, MgO-coated and Si/MgO-coated after 3, 7, and 9 days.

It is known that Mg alloys without any surface modification will be seriously degraded in contact with the medium. The degradation process is followed by the production of hydrogen, Mg^{2+}, and OH^- which, in turn, raises the concentration of Mg ions and the pH value of the medium. Rapid degradation of Mg-based alloys accompanied by the release of hydrogen bubbles is detrimental to cell culture and prevents the survival and growth of cultured cells. As the cells would be pushed away from the substrate surface by the continuous release of H_2, the cell adhesion on the sample surfaces in vitro and in vivo would be inhibited. Moreover, clinical application of Mg-based implants was hindered owing to their mechanical integrity loss by the rapid degradation rate before sufficiently healing the damaged bone. As can be seen in Figure 15, the cell viability percentage improved by increasing the incubation time as, after nine days, it reached 72, 71, and 84 for uncoated, MgO-coated, and Si/MgO-coated, respectively. This enhancement can be attributed to the decline of the very fast initial degradation rate of the Mg-based nanocomposite by the formation of corrosion products that act as the protective coverage against corrosive media. Therefore, excessive formation of hydrogen bubbles, released metal ions, and an alkaline environment that resulted from the rapid degradation of Mg-based samples are restricted by the precipitation of corrosion products on the surface of the samples. As cells are very sensitive to environmental fluctuations, MgO and Si/MgO coatings provide an environment with a closer pH to the normal physiological environment by controlling the rapid corrosion rate of the Mg-based nanocomposite, thus benefitting cell adhesion and growth. During degradation of the samples, smaller amounts of Mg and alloying elements can be released from the coated samples, thus giving rise to better cell viability and cell attachment rather than the uncoated sample. As better cell viability and cell attachment are achieved when the cells are cultured in a friendly environment

with less adverse stimulation and pH value, hydrogen evolution may negatively influence direct cell adhesion [52]. Therefore, less hydrogen evolution by Si/MgO and MgO coatings provide more stable surfaces with better biocompatibility than the bare nanocomposite.

Figure 16 shows the FE-SEM morphology of the cultured cells for 72 h on the surfaces of uncoated, MgO-coated, and Si/MgO-coated, which clearly indicates the adhered cells on the surfaces. Areas occupied by the cells on the surface are shown in Figure 16 by arrows. With regards to the FE-SEM micrographs and cell viability test, the Si/MgO-coated nanocomposite exhibits good cell adhesion and viability. This is possibly because of the formation of anti-corrosion, and biocompatible surface coatings containing Si and MgO layers, which provide a more stable and favorable environment for cell attachment and cell growth.

As can be observed in Figure 16, the NHost cells cultured on the uncoated sample spread less and also have a more abnormal shape compared to cells, which adhered and spread well on the MgO-coated with a normal shape. The NHost cells cultured on the surface of the Si/MgO-coated are large in number and spread very well with three days of incubation. There is a higher tendency of better proliferation among the cells that spread better, as good cell attachment is an important parameter for promoting proliferation [52].
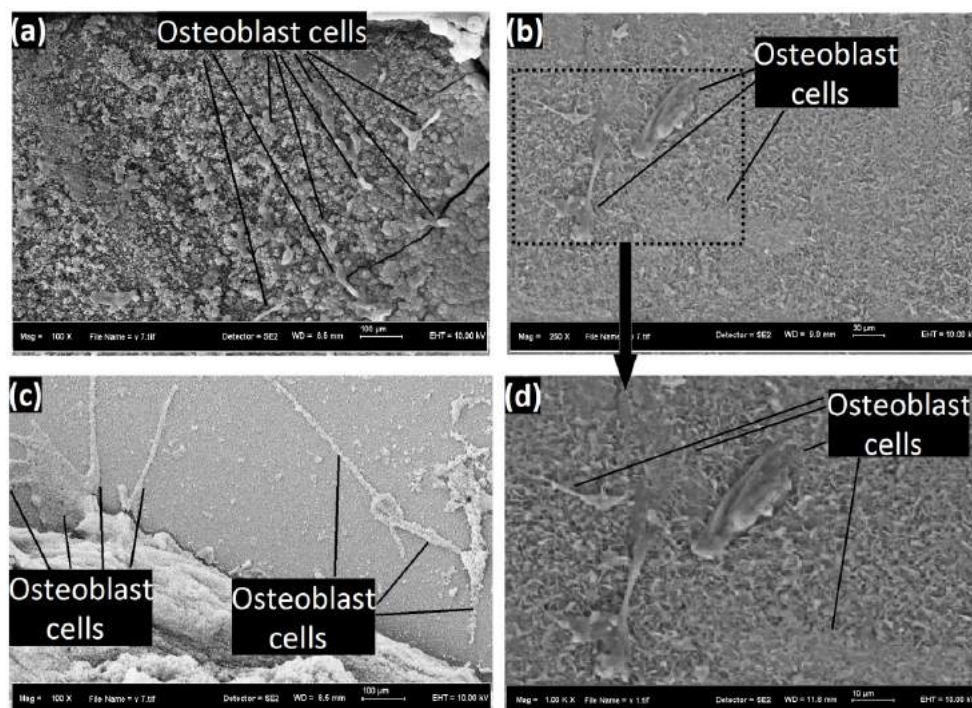

Figure 16. FE-SEM micrographs of the cells cultured for 3 days on the surfaces of (**a**) uncoated, (**b**) MgO-coated and (**c**,**d**) Si/MgO-coated, which evidently indicate the adhered cells on the surfaces (arrows).

4. Conclusions

MgO-coated and Si/MgO-coated were fabricated using the ball-milling multi-step cold-pressing sintering powder metallurgy (PM) technique. The XRD, EDS, XPS, and FE-SEM results confirmed that monolayer MgO and double-layer Si/MgO as the protective coatings bonded onto the surface of Mg/HA/TiO$_2$ bionanocomposite to control the degradation rate in a physiological corrosive environment. Potentiodynamic polarization, electrochemical impedance spectroscopy, and immersion tests supported that the anticorrosion ability of Mg/HA/TiO$_2$ was improved significantly after surface modification. The smaller corrosion current densities and higher impedance in SBF were displayed by the coated samples. Less hydrogen evolution and much less severe corrosion are observed for

the Si/MgO-coated. The remarkable enhancement in the corrosion resistance is mainly attributed to the stable and protective Si outer layer, as well as the partially-protective MgO inner layer. In vitro immersion testing in simulated body fluid within seven days of immersion demonstrated that the MgO and Si/MgO coating possesses a good biomineralization performance. With regards the biological tests, cells attach and spread well on the Si/MgO-coated and cells incubated with the extracted medium of the Si/MgO-coated show closer viability to the value obtained from the complete cell culture medium compared to those of the uncoated and MgO-coated. This indicates that the Si/MgO-coated has good biocompatibility in vitro. The improvement in the in vitro biological response cells resulted from the improved corrosion resistance. Si/MgO is a promising method to improve both the corrosion resistance and in vitro biocompatibility of the $Mg/HA/TiO_2$ bionanocomposite based on our results.

Author Contributions: Shahrouz Zamani Khalajabadi designed and prepared most parts of the experiments and wrote the main part of the manuscript. Aminudin Haji Abu edited the entire manuscript and selected the required experiments. Norhayati Ahmad worked on the XRD, FE-SEM, EDS spectral data together with the measurement of bonding strength of coatings to the substrate. Norizah Bt Hj Redzuan carried out XPS analysis. Mohammad Rafiq Abdul Kadir contributed to the biocorrosion sections (experiments and analysis). The main part of the biological experiments, and the related discussion on biological terms were performed by Rozita Nasiri. Ahmad Fauzi Ismail contributed to the AFM part and to the roughness measurement of sample surfaces. The English of the manuscript was substantially edited by Waseem Haider, who also helped to write and discuss the biological section.

Conflicts of Interest: The authors declare no conflict of interest.

References

1. Yahata, C.; Mochizuki, A. Platelet compatibility of magnesium alloys. *Mater. Sci. Eng. C* **2017**, *78*, 1119–1124. [CrossRef] [PubMed]
2. Zheng, Y.F.; Gu, X.N.; Witte, F. Biodegradable metals. *Mater. Sci. Eng. R Rep.* **2014**, *77*, 1–34. [CrossRef]
3. Rosalbino, F.; De Negri, S.; Saccone, A.; Angelini, E.; Delfino, S. Bio-corrosion characterization of Mg-Zn-X (*X* = Ca, Mn, Si) alloys for biomedical applications. *J. Mater. Sci. Mater. Med.* **2010**, *21*, 1091–1098. [CrossRef] [PubMed]
4. Wolf, F.I.; Cittadini, A. Chemistry and biochemistry of magnesium. *Mol. Asp. Med.* **2003**, *24*, 3–9. [CrossRef]
5. Zhang, S.; Zhang, X.; Zhao, C.; Li, J.; Song, Y.; Xie, C.; Tao, H.; Zhang, Y.; He, Y.; Jiang, Y.; et al. Research on an Mg-Zn alloy as a degradable biomaterial. *Acta Biomater.* **2010**, *6*, 626–640. [CrossRef] [PubMed]
6. Song, G. Control of biodegradation of biocompatable magnesium alloys. *Corros. Sci.* **2007**, *49*, 1696–1701. [CrossRef]
7. Kayhan, S.M.; Tahmasebifar, A.; Koç, M.; Usta, Y.; Tezcaner, A.; Evis, Z. Experimental and numerical investigations for mechanical and microstructural characterization of micro-manufactured AZ91D magnesium alloy disks for biomedical applications. *Mater. Des.* **2016**, *93*, 397–408. [CrossRef]
8. Jiang, H.; Wang, J.; Chen, M.; Liu, D. Biological activity evaluation of magnesium fluoride coated Mg-Zn-Zr alloy in vivo. *Mater. Sci. Eng. C* **2017**, *75*, 1068–1074. [CrossRef] [PubMed]
9. Adekanmbi, I.; Mosher, C.Z.; Lu, H.H.; Riehle, M.; Kubba, H.; Tanner, E. Mechanical behaviour of biodegradable AZ31 magnesium alloy after long term in vitro degradation. *Mater. Sci. Eng. C* **2017**, *77*, 1135–1144. [CrossRef] [PubMed]
10. Minárik, P.; Jablonská, E.; Král, R.; Lipov, J.; Ruml, T.; Blawert, C.; Hadzima, B.; Chmelík, F. Effect of equal channel angular pressing on in vitro degradation of LAE442 magnesium alloy. *Mater. Sci. Eng. C* **2017**, *73*, 736–742. [CrossRef] [PubMed]
11. Chen, Y.; Yan, G.; Wang, X.; Qian, H.; Yi, J.; Huang, L.; Liu, P. Bio-functionalization of micro-arc oxidized magnesium alloys via thiol-ene photochemistry. *Surf. Coat. Technol.* **2015**, *269*, 191–199. [CrossRef]
12. Kokubo, T.; Takadama, H. How useful is SBF in predicting in vivo bone bioactivity? *Biomaterials* **2006**, *27*, 2907–2915. [CrossRef] [PubMed]
13. Kokubo, T. Bioactive glass ceramics: Properties and applications. *Biomaterials* **1991**, *12*, 155–163. [CrossRef]

14. Al-Noaman, A.; Rawlinson, S.C.; Hill, R.G. The role of MgO on thermal properties, structure and bioactivity of bioactive glass coating for dental implants. *J. Noncryst. Solids* **2012**, *358*, 3019–3027. [CrossRef]

15. Bakhsheshi-Rad, H.R.; Hamzah, E.; Kasiri-Asgarani, M.; Jabbarzare, S.; Iqbal, N.; Abdul Kadir, M.R. Deposition of nanostructured fluorine-doped hydroxyapatite-polycaprolactone duplex coating to enhance the mechanical properties and corrosion resistance of Mg alloy for biomedical applications. *Mater. Sci. Eng. C* **2016**, *60*, 526–537. [CrossRef] [PubMed]

16. Shangguan, Y.; Sun, L.; Wan, P.; Tan, L.; Wang, C.; Fan, X.; Qin, L.; Yang, K. Comparison study of different coatings on degradation performance and cell response of Mg-Sr alloy. *Mater. Sci. Eng. C* **2016**, *69*, 95–107. [CrossRef] [PubMed]

17. Agarwal, S.; Curtin, J.; Duffy, B.; Jaiswal, S. Biodegradable magnesium alloys for orthopaedic applications: A review on corrosion, biocompatibility and surface modifications. *Mater. Sci. Eng. C* **2016**, *68*, 948–963. [CrossRef] [PubMed]

18. Pan, C.-J.; Hou, Y.; Wang, Y.-N.; Gao, F.; Liu, T.; Hou, Y.; Zhu, Y.; Ye, W.; Wang, L. Effects of self-assembly of 3-phosphonopropionic acid, 3-aminopropyltrimethoxysilane and dopamine on the corrosion behaviors and biocompatibility of a magnesium alloy. *Mater. Sci. Eng. C* **2016**, *67*, 132–143. [CrossRef] [PubMed]

19. Kang, M.H.; Jang, T.S.; Kim, S.W.; Park, H.S.; Song, J.; Kim, H.; Jung, K.; Jung, H. MgF_2-coated porous magnesium/alumina scaffolds with improved strength, corrosion resistance, and biological performance for biomedical applications. *Mater. Sci. Eng. C* **2016**, *62*, 634–642. [CrossRef] [PubMed]

20. Levy, G.K.; Ventura, Y.; Goldman, J.; Vago, R.; Aghion, E. Cytotoxic characteristics of biodegradable EW10X04 Mg alloy after Nd coating and subsequent heat treatment. *Mater. Sci. Eng. C* **2016**, *62*, 752–761. [CrossRef] [PubMed]

21. Lin, X.; Tan, L.; Wang, Q.; Zhang, G.; Zhang, B.; Yang, K. In vivo degradation and tissue compatibility of ZK60 magnesium alloy with micro-arc oxidation coating in a transcortical model. *Mater. Sci. Eng. C* **2013**, *33*, 3881–3888. [CrossRef] [PubMed]

22. Gu, X.N.; Li, N.; Zhou, W.R.; Zheng, Y.F.; Zhao, X.; Cai, Q.Z.; Ruan, L. Corrosion resistance and surface biocompatibility of a microarc oxidation coating on a Mg–Ca alloy. *Acta. Biomater.* **2011**, *7*, 1880–1889. [CrossRef] [PubMed]

23. Pan, Y.; He, S.; Wang, D.; Huang, D.; Zheng, T.; Wang, S.; Dong, P.; Chen, C. In vitro degradation and electrochemical corrosion evaluations of microarc oxidized pure Mg, Mg–Ca and Mg–Ca–Zn alloys for biomedical applications. *Mater. Sci. Eng. C* **2015**, *47*, 85–96. [CrossRef] [PubMed]

24. Dinu, M.; Ivanova, A.A.; Surmeneva, M.A.; Braic, M.; Tyurin, A.I.; Braic, V.; Surmenev, R.A.; Vladescu, A. Tribological behaviour of RF-magnetron sputter deposited hydroxyapatite coatings in physiological solution. *Ceram. Int.* **2017**, *43*, 6858–6867. [CrossRef]

25. Khalajabadi, S.Z.; Ahmad, N.; Izman, S.; Abu, A.B.H.; Haider, W.; Kadir, M.R.A. In vitro biodegradation, electrochemical corrosion evaluations and mechanical properties of an $Mg/HA/TiO_2$ nanocomposite for biomedical applications. *J. Alloys Compd.* **2017**, *696*, 768–781. [CrossRef]

26. Yang, L.; Ma, L.; Huang, Y.; Feyerabend, F.; Blawert, C.; Höche, D.; Willumeit-Römer, R.; Zhang, E.; Kainer, K.U.; Hort, N. Influence of Dy in solid solution on the degradation behavior of binary Mg-Dy alloys in cell culture medium. *Mater. Sci. Eng. C* **2017**, *75*, 1351–1358. [CrossRef] [PubMed]

27. Zhang, S.; Zheng, Y.; Zhang, L.; Bi, Y.; Li, J.; Liu, J.; Yu, Y.; Guo, H.; Li, Y. In vitro and in vivo corrosion and histocompatibility of pure Mg and a Mg-6Zn alloy as urinary implants in rat model. *Mater. Sci. Eng. C* **2016**, *68*, 414–422. [CrossRef] [PubMed]

28. Paital, S.R.; Dahotre, N.B. Calcium phosphate coatings for bio-implant applications: Materials, performance factors, and methodologies. *Mater. Sci. Eng. R Rep.* **2009**, *66*, 1–70. [CrossRef]

29. Li, J.; Song, Y.; Zhang, S.; Zhao, C.; Zhang, F.; Cao, L.; Fan, Q.; Tang, T. In vitro responses of human bone marrow stromal cells to a fluoridated hydroxyapatite coated biodegradable Mg–Zn alloy. *Biomaterials* **2010**, *31*, 5782–5788. [CrossRef] [PubMed]

30. Heublein, B.; Rohde, R.; Kaese, V.; Niemeyer, M.; Hartung, W.; Haverich, A. Biocorrosion of magnesium alloys: A new principle in cardiovascular implant technology? *Heart* **2003**, *89*, 651–656. [CrossRef] [PubMed]

31. Zartner, P.; Buettner, M.; Singer, H.; Sigler, M. First biodegradable metal stent in a child with congenital heart disease: Evaluation of macro and histopathology. *Catheter. Cardiovasc. Interv.* **2007**, *69*, 443–446. [CrossRef] [PubMed]

32. Gu, X.; Zhou, W.; Zheng, Y.; Dong, L.; Xi, Y.; Chai, D. Microstructure, mechanical property, bio-corrosion and cytotoxicity evaluations of Mg/HA composites. *Mater. Sci. Eng. C* **2010**, *30*, 827–832. [CrossRef]

33. Khalajabadi, S.Z.; Ahmad, N.; Yahya, A.; Yajid, M.; Samavati, A.; Asadi, S.; Arafat, A.; Kadir, M.R.A. The role of titania on the microstructure, biocorrosion and mechanical properties of Mg/HA-based nanocomposites for potential application in bone repair. *Ceram. Int.* **2016**, *42*, 18223–18237. [CrossRef]

34. Li, M.; Cheng, Y.; Zheng, Y.; Zhang, X.; Xi, T.; Wei, S. Plasma enhanced chemical vapor deposited silicon coatings on Mg alloy for biomedical application. *Surf. Coat. Technol.* **2013**, *228*, S262–S265. [CrossRef]

35. Khalajabadi, S.Z.; Abdul Kadir, M.R.; Izman, S.; Samavati, A.; Othaman, Z. Synthesis, microstructure and biodegradation behavior of nano-Si and nano-ZnO/Si coatings on a Mg/HA/TiO$_2$/MgO nanocomposite. *Ceram. Int.* **2015**, *41*, 11346–11358. [CrossRef]

36. Khan, A.F.; Saleem, M.; Afzal, A.; Ali, A.; Khan, A.; Khan, A.R. Bioactive behavior of silicon substituted calcium phosphate based bioceramics for bone regeneration. *Mater. Sci. Eng. C* **2014**, *35*, 245–252. [CrossRef] [PubMed]

37. Carlisle, E.M. Silicon: A possible factor in bone calcification. *Science* **1970**, *167*, 279–280. [CrossRef] [PubMed]

38. Schwarz, K.; Milne, D.B. Growth-promoting effects of silicon in rats. *Nature* **1972**, *239*, 333–334. [CrossRef] [PubMed]

39. Wu, C.; Chang, J. Degradation, bioactivity, and cytocompatibility of diopside, akermanite, and bredigite ceramics. *J. Biomed. Mater. Res.* **2007**, *83*, 153–160. [CrossRef] [PubMed]

40. Wang, Q.; Tan, L.; Yang, K. Cytocompatibility and Hemolysis of AZ31B Magnesium Alloy with Si-containing Coating. *J. Mater. Sci. Technol.* **2015**, *31*, 845–851. [CrossRef]

41. Shi, P.; Niu, B.; Chen, Y.; Li, Q. Preparation and characterization of PLA coating and PLA/MAO composite coatings on AZ31 magnesium alloy for improvement of corrosion resistance. *Surf. Coat. Technol.* **2015**, *262*, 26–32. [CrossRef]

42. Brink, M. The influence of alkali and alkaline earths on the working range for bioactive glasses. *J. Biomed. Mater. Res.* **1997**, *36*, 109–117. [CrossRef]

43. Watts, S.J.; Hill, R.G.; O'Donnell, M.D.; Law, R.V. Influence of magnesia on the structure and properties of bioactive glasses. *J. Noncryst. Solids* **2010**, *356*, 517–524. [CrossRef]

44. Ebisawa, Y.; Kokubo, T.; Ohura, K.; Yamamuro, T. Bioactivity of CaO·SiO2-based glasses: In vitro evaluation. *J. Mater. Sci. Mater. Med.* **1990**, *1*, 239–244. [CrossRef]

45. Kasuga, T.; Nakagawa, K.; Yoshida, M.; Miyade, E. Compositional dependence of formation of an apatite layer on glass-ceramics in simulated physiological solution. *J. Mater. Sci.* **1987**, *22*, 3721–3724. [CrossRef]

46. Oliveira, J.M.; Correia, R.N.; Fernandes, M.H.; Rocha, J. Influence of the CaO/MgO ratio on the structure of phase-separated glasses: a solid state 29Si and 31P MAS NMR study. *J. Noncryst. Solids* **2000**, *265*, 221–229. [CrossRef]

47. *ASTM1147-F Standard Test Method for Tension Testing of Coatings*; ASTM International: West Conshohocken, PA, USA, 2005.

48. Amiri, H.; Mohammadi, I.; Afshar, A. Electrophoretic deposition of nano-zirconia coating on AZ91D magnesium alloy for bio-corrosion control purposes. *Surf. Coat. Technol.* **2017**, *311*, 182–190. [CrossRef]

49. *ASTM D4541-17 Standard Test Method for Pull-Off Strength of Coatings Using Portable Adhesion Testers*; ASTM International: West Conshohocken, PA, USA, 2017.

50. Sudholz, A.; Gusieva, K.; Chen, X.; Muddle, B.; Gibson, M.; Birbilis, N. Electrochemical behaviour and corrosion of Mg–Y alloys. *Corros. Sci.* **2011**, *53*, 2277–2282. [CrossRef]

51. Qi, G.; Zhang, S.; Khor, K.A.; Weng, W.; Zeng, X.; Liu, C. An interfacial study of sol–gel-derived magnesium apatite coatings on Ti6Al4V substrates. *Thin Solid Films* **2008**, *516*, 5172–5175. [CrossRef]

52. Jin, W.; Wu, G.; Feng, H.; Wang, W.; Zhang, X.; Chu, P.K. Improvement of corrosion resistance and biocompatibility of rare-earth WE43 magnesium alloy by neodymium self-ion implantation. *Corros. Sci.* **2015**, *94*, 142–155. [CrossRef]

53. Gu, C.D.; Yan, W.; Zhang, J.L.; Tu, J.P. Corrosion resistance of AZ31B magnesium alloy with a conversion coating produced from a choline chloride—Urea based deep eutectic solvent. *Corros. Sci.* **2016**, *106*, 108–116. [CrossRef]

54. Li, Z.; Yuan, Y.; Jing, X. Composite coatings prepared by combined plasma electrolytic oxidation and chemical conversion routes on magnesium-lithium alloy. *J. Alloys Compd.* **2017**, *706*, 419–429. [CrossRef]

55. Wang, M.J.; Li, C.F.; Yen, S.K. Electrolytic MgO/ZrO$_2$ duplex-layer coating on AZ91D magnesium alloy for corrosion resistance. *Corros. Sci.* **2013**, *76*, 142–153. [CrossRef]
56. Taleatu, B.A.; Omotoso, E.; Lal, C.; Makinde, W.O.; Ogundele, K.T.; Ajenifuja, E.; Lasisi, A.R.; Eleruja, M.A.; Mola, G.T. XPS and some surface characterizations of electrodeposited MgO nanostructure. *Surf. Interface Anal.* **2014**, *46*, 372–377. [CrossRef]
57. Zhang, D.; Wei, B.; Wu, Z.; Qi, Z.; Wang, Z. A comparative study on the corrosion behaviour of Al, Ti, Zr and Hf metallic coatings deposited on AZ91D magnesium alloys. *Surf. Coat. Technol.* **2016**, *303*, 94–102. [CrossRef]
58. Chang, J.K.; Chen, S.Y.; Tsai, W.T.; Deng, M.J.; Sun, I.W. Electrodeposition of aluminum on magnesium alloy in aluminum chloride (AlCl$_3$)–1-ethyl-3-methylimidazolium chloride (EMIC) ionic liquid and its corrosion behavior. *Electrochem. Commun.* **2007**, *9*, 1602–1606. [CrossRef]
59. Ryu, H.; Sheng, N.; Ohtsuka, T.; Fujita, S.; Kajiyama, H. Polypyrrole film on 55% Al–Zn-coated steel for corrosion prevention. *Corros. Sci.* **2012**, *56*, 67–77. [CrossRef]
60. Gu, K.; Lv, L.; Lu, Z.; Yang, H.; Mao, F.; Tang, J. Electrochemical corrosion and impedance study of SAE1045 steel under gel-like environment. *Corros. Sci.* **2013**, *74*, 408–413. [CrossRef]
61. Chen, Z.; Huang, L.; Zhang, G.; Qiu, Y.; Guo, X. Benzotriazole as a volatile corrosion inhibitor during the early stage of copper corrosion under adsorbed thin electrolyte layers. *Corros. Sci.* **2012**, *65*, 214–222. [CrossRef]
62. Shi, Z.; Liu, M.; Atrens, A. Measurement of the corrosion rate of magnesium alloys using Tafel extrapolation. *Corros. Sci.* **2010**, *52*, 579–588. [CrossRef]
63. Zhao, L.; Cui, C.; Wang, Q.; Bu, S. Growth characteristics and corrosion resistance of micro-arc oxidation coating on pure magnesium for biomedical applications. *Corros. Sci.* **2010**, *52*, 2228–2234. [CrossRef]
64. Wang, C.; Jiang, B.; Liu, M.; Ge, Y. Corrosion characterization of micro-arc oxidization composite electrophoretic coating on AZ31B magnesium alloy. *J. Alloys Compd.* **2015**, *621*, 53–61. [CrossRef]
65. Choi, H.Y.; Kim, W.J. Development of the highly corrosion resistant AZ31 magnesium alloy by the addition of a trace amount of Ti. *J. Alloys Compd.* **2016**, *664*, 25–37. [CrossRef]
66. Khalajabadi, S.Z.; Kadir, M.R.A.; Izman, S.; Bakhsheshi-Rad, H.R.; Farahany, S. Effect of mechanical alloying on the phase evolution, microstructure and bio-corrosion properties of a Mg/HA/TiO$_2$/MgO nanocomposite. *Ceram. Int.* **2014**, *40*, 16743–16759. [CrossRef]
67. Shi, Y.; Qi, M.; Chen, Y.; Shi, P. AO-DCPD composite coating on Mg alloy for degradable implant applications. *Mater. Lett.* **2011**, *65*, 2201–2204. [CrossRef]
68. Han, J.; Wan, P.; Sun, Y.; Liu, Z.; Fan, X.; Tan, L.; Yang, K. Fabrication and evaluation of a bioactive Sr-Ca-P contained micro-arc oxidation coating on magnesium strontium alloy for bone repair application. *J. Mater. Sci. Technol.* **2016**, *32*, 233–244. [CrossRef]
69. Zhang, J.; Kong, N.; Shi, Y.; Niu, J.; Mao, L.; Li, H.; Xiong, M.; Yuan, G. Influence of proteins and cells on in vitro corrosion of Mg–Nd–Zn–Zr alloy. *Corros. Sci.* **2014**, *85*, 477–481. [CrossRef]
70. Wang, H.; Zhu, S.; Wang, L.; Feng, Y.; Ma, X.; Guan, S. Formation mechanism of Ca-deficient hydroxyapatite coating on Mg–Zn–Ca alloy for orthopaedic implant. *Appl. Surf. Sci.* **2014**, *307*, 92–100. [CrossRef]
71. Yao, Z.Q.; Ivanisenko, Y.; Diemant, T.; Caron, A.; Chuvilin, A.; Jiang, J.Z.; Valiev, R.Z.; Qi, M.; Fecht, H.-J. Synthesis and properties of hydroxyapatite-containing porous titania coating on ultrafine-grained titanium by micro-arc oxidation. *Acta. Biomater.* **2010**, *6*, 2816–2825. [CrossRef] [PubMed]
72. El-Hadad, A.A.; Barranco, V.; Samaniego, A.; Llorente, I.; García-Galván, F.; Jiménez-Morales, A.; Galván, J.C.; Feliu, S., Jr. Influence of substrate composition on corrosion protection of sol–gel thin films on magnesium alloys in 0.6 M NaCl aqueous solution. *Prog. Org. Coat.* **2014**, *77*, 1642–1652. [CrossRef]
73. Li, H.; Pang, S.; Liu, Y.; Sun, L.; Liaw, P.K.; Zhang, T. Biodegradable Mg–Zn–Ca–Sr bulk metallic glasses with enhanced corrosion performance for biomedical applications. *Mater. Des.* **2015**, *67*, 9–19. [CrossRef]
74. Hornberger, H.; Virtanen, S.; Boccaccini, A.R. Biomedical coatings on magnesium alloys—A review. *Acta Biomater.* **2012**, *8*, 2442–2455. [CrossRef] [PubMed]
75. Shadanbaz, S.; Dias, G.J. Calcium phosphate coatings on magnesium alloys for biomedical applications: A review. *Acta. Biomater.* **2012**, *8*, 20–30. [CrossRef] [PubMed]